Integrative Biology

PAPER

View Article Online
View Journal | View Issue

Cite this: *Integr. Biol.*, 2015, 7, 1186

Quantifying cell-induced matrix deformation in three dimensions based on imaging matrix fibers†

Jacob Notbohm,‡[a] Ayelet Lesman,‡[b] David A. Tirrell[b] and Guruswami Ravichandran*[a]

Received 17th January 2015,
Accepted 19th May 2015

DOI: 10.1039/c5ib00013k

www.rsc.org/ibiology

During processes such as development and cancer metastasis, cells migrate into three-dimensional fibrous matrices. Previous studies have speculated on the mechanical forces required for migration by observing matrix fiber alignment, densification, and degradation, but these forces remain difficult to quantify. Here we present a new experimental technique to simultaneously measure full-field 3D displacements and structural remodeling of a fibrous matrix, both of which result from cellular forces. We apply this "2-in-1" experimental technique to follow single cells as they invade a physiologically relevant fibrin matrix. We find that cells generate tube-like structures in the matrix by plastically deforming their surroundings, and they re-use these tubes to extend protrusions. Cells generate these tubular structures by applying both pulling and pushing forces.

Insight, innovation, integration

Many cell types adhere to and migrate within a three-dimensional fibrous matrix. Despite the fact that cells respond to deformation of the matrix, there are limited tools available to probe cell–matrix interactions in a non-invasive fashion. Previous experiments have either imaged matrix fibers without measuring deformations or measured matrix deformations without visualizing matrix fibers. Here we present a new "2-in-1" technique that uses the fibrous structure of the matrix to quantify matrix deformations while simultaneously providing microstructural details on the remodeled matrix in all three dimensions. Using our technique we quantify matrix deformations applied by invading cells to create track-like void spaces for migration. We find that the cells form these tracks by both pulling and pushing on the matrix.

Introduction

Three-dimensional (3D) fibrous gels such as collagen and fibrin are important *in vitro* culture systems to study cellular processes in tissue-like environments.[1] Cells embedded in these matrices apply traction forces against their local surroundings, remodeling the matrix to create heterogeneous meshes of fibers at the cellular level. Such forces combined with the mechanical signals from the remodeled matrix direct key cellular processes such as cellular migration,[2] embryonic and tissue development,[3] and cancer progression.[4] Recent studies have quantified 3D tractions applied by cells grown on artificial flat substrates[5–8] and within synthetic polyethylene glycol gels.[9] Other studies have inferred cell tractions in fibrous matrices by quantifying local matrix displacements[10–12] or global matrix strains,[13] or by assuming that the fibrous matrix behaves as a linear material.[14,15]

While these previous experiments in fibrous materials have provided approximate measures of cell contractile activity, they have failed to track the associated microstructural changes in the matrix. Visualizing the fibrillar matrix by live-cell microscopy can provide direct insight into mechanisms of matrix remodeling events such as matrix deposition, degradation and deformation, all of which play important roles *in vivo*.[16] For example, highly remodeled extracellular matrix zones in collagen gels provide pathways for cell motility, prompting the transition toward collective cancer cell invasion.[16] Thus, imaging of matrix remodeling coupled with mechanical measurements of cell contractility offers the prospect of deeper understanding of 3D cell–matrix interactions.

Here, we combine a direct measurement of matrix deformations with time lapse imaging of the matrix microstructure. We demonstrate the use of microstructural imaging through a series of controlled loading experiments, and we apply our "2-in-1" microstructural-mechanical imaging technique to investigate invasion, an early stage of cell migration in a fibrous matrix. During invasion, cells align[17] and degrade[18] the matrix fibers,

[a] *Division of Engineering and Applied Science, California Institute of Technology, Pasadena, CA, USA. E-mail: ravi@caltech.edu*
[b] *Division of Chemistry and Chemical Engineering, California Institute of Technology, Pasadena, CA, USA*

† Electronic supplementary information (ESI) available. See DOI: 10.1039/c5ib00013k

‡ These authors contributed equally to this work.

resulting in an extracellular environment that changes in time and space. We dynamically quantify both the matrix microstructural changes and the cell-induced deformations. We find large plastic deformation of the matrix, generated by a combination of pushing and pulling forces that cells use to invade the matrix meshwork.

Results

We have developed a new experimental technique to record matrix microstructural changes and quantify cell-generated matrix deformations simultaneously. Our matrix microstructural imaging makes use of a fluorescent label on the matrix fibers of a fibrin gel, which provides high contrast and accurate images for fibers of all orientations in three-dimensional space.[19] The high contrast of the fiber images allows computation of matrix deformations with digital volume correlation (DVC).[20] The DVC segments the entire matrix volume into $\sim 25\ \mu m^3$ subsets (Fig. 1a). It then correlates these 3D subsets to compute full-field 3D deformations of the matrix at a high level of precision and spatial resolution of 8 μm. The typical experimental noise level in this system is 0.05 μm of displacement (Fig. 1b) and 0.1% strain (Fig. 1c). We find similar noise levels for gels made with fibrinogen densities ranging from 2 to 6 mg mL^{-1} (Fig. S1, ESI†). The accuracy of our displacement measurement is roughly 0.2 μm for displacements ranging from 1 to 5 μm, a typical range for cell-induced deformations (Fig. S1, ESI†).

We encapsulated in the fibrin matrix 3T3 fibroblast cells that stably express an actin-GFP fusion protein. The fibroblasts exert forces against their surrounding matrix and reorganize matrix fibers around them, as shown by an increase in fluorescence intensity due to densification of fibers (Fig. 1d and e). Using our DVC approach, we used the inhomogeneous fluorescence pattern of the fibers to measure matrix displacements in all three spatial dimensions. The correlation reveals that cell-induced displacements are directed toward the long axis of the cell body, with the largest displacements concentrated near thin cellular extensions (Fig. 1e). Most regions of large matrix displacement correlate with areas of increased fiber density (bright fluorescence) and alignment as compared to areas distal to the cell, which exhibit random arrangements of fibers (Fig. 1d). To test the impact of the observed local matrix remodeling on the performance of the DVC, we conducted a series of numerical experiments. In these experiments, we computationally included bright spots (representing fiber densification) or holes (representing fiber degradation) to a single subvolume used for the correlation and measured the accuracy of the DVC by correlating the modified subvolume to an unmodified reference one (Fig. S2, ESI†). These spots induce errors only when they take up more than 3% of the voxels within a subvolume (Fig. S2, ESI†).

Structural remodeling of the matrix due to cellular forces is a complex process, in part because fibrin gels are not linearly elastic. Bulk specimens of the fibrin matrix exhibit low shear storage moduli G' (30–40 Pa, Fig. 2), characteristic of compliant

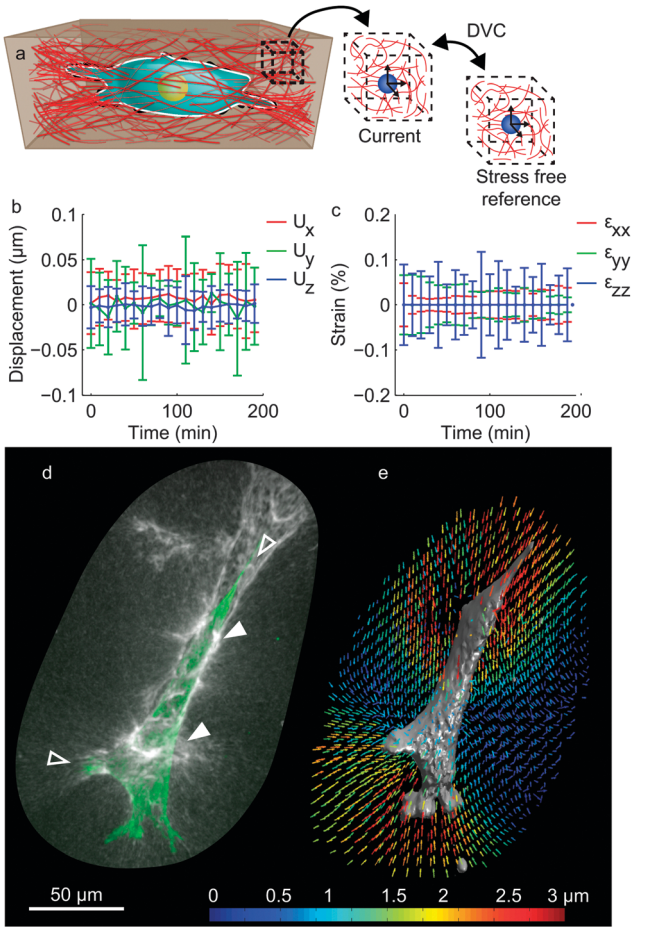

Fig. 1 Microstructural-mechanical image correlation measures full-field 3D displacements by correlating displacements in matrix fibers over time. (a) The illustration shows a 3D view of a fibrous matrix around a cell. Displacements are measured by correlating cubic subvolumes between reference and current (deformed) states with DVC. (b, c) Time lapse cell-free control experiments showing the noise-level for displacements U (b) and strains ε (c) with components in the x, y, and z directions. The plots present mean ± standard deviation of a fluorescently labeled-fibrin matrix in concentration of 4 mg mL^{-1} fibrinogen. (d) A fibroblast (actin, green) rearranges the matrix (gray) around the cell body (solid arrows) and around cell extensions (hollow arrows). Matrix fibers align near the cellular extensions but not in regions away from the cell. (e) The cell applies displacements to the matrix primarily near the extensions along its axis.

tissues such as mammary gland and brain.[21] Inspection of the shear loss modulus G'' shows that fibrin gels exhibit viscoelastic behavior with large loss tangents, $\tan\delta = G''/G'$, of ~ 0.5 (Fig. 2). In addition, fibrous materials are known to exhibit strain stiffening in shear,[22] negative effective bulk moduli in tension,[23] and loss of strength in compression due to fiber buckling.[24] To further complicate the mechanics of the fibrous matrix, cells actively align (Fig. 1d), stiffen,[25] and degrade the matrix fibers.[26] In summary, the response of the fibrous matrix to cell-induced forces is nonlinear, local, viscoelastic, anisotropic, and time-dependent.

To relate matrix deformation to changes in matrix microstructure, we first performed a series of cell-free control experiments (Fig. 3). Rigid spherical poly(methyl methacrylate) particles

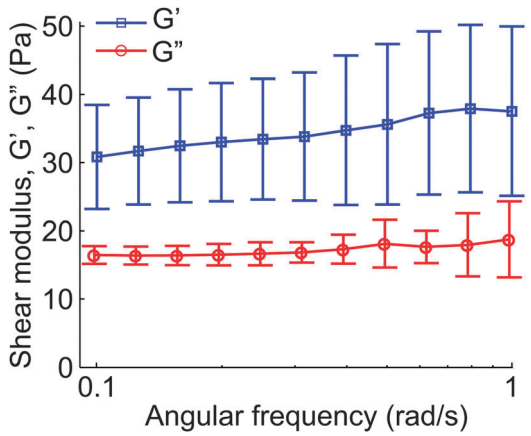

Fig. 2 Constitutive properties of labeled fibrin gels (4 mg mL^{-1} fibrinogen) were measured with a rheometer. The shear storage modulus G' is approximately 33 Pa over a range of frequencies. If Poisson's ratio is 0.5, this corresponds to a Young's modulus of 100 Pa. The loss modulus G'' is roughly half the storage modulus, indicating the material is viscoelastic with a loss tangent $\tan\delta = G''/G'$, of $\sim$0.5. Each point shows the mean of four different samples; error bars are standard deviation.

(diameter 45 μm) were encapsulated in fluorescently labeled fibrin matrices. The matrix fibers were imaged by confocal microscopy during uniaxial compression in a loading apparatus similar to that described previously.[20] The stress concentration factor (ratio of local stress to far field stress), computed from linear elasticity,[27] on the surface of the sphere is plotted in Fig. 3b. Uniaxial compression creates compressive stress in the matrix at the north and south poles of the sphere and tensile stress along the equatorial plane. Regions of the matrix near the poles of the sphere, which are under large compressive stress, become dense and compacted as shown by increased fluorescence intensity compared with regions farther from the sphere (Fig. 3c, $z = -32$, -24 μm). In contrast, matrix intensity decreases in regions of the matrix near the equator of the sphere (Fig. 3c, $z = 0$, 8 μm). The reduction in fluorescence intensity near the equator indicates tensile stresses within the matrix. These tensile stresses decrease with distance from the sphere, corresponding to an increase in fluorescence intensity in a strain-dependent manner (Fig. 3d). To relate fluorescence intensity to matrix density, we compare to the linear elastic scaling relationship $\rho_2/\rho_1 = (1 + Cr^{-3})^{-1}$ where r is distance from the center of the sphere, C is a fitting constant, and the ratio ρ_2/ρ_1 is the ratio of fluorescence intensity near the sphere to far from the sphere (see supplemental note for more detail, ESI†). The fluorescence intensity matches this scaling relationship well, except for fluctuations due to inhomogeneities in the matrix and systematic deviations at large strains due to nonlinearity (Fig. 3d). These direct observations of matrix fluorescence intensity demonstrate the value of microstructural imaging for revealing the stress state in the matrix.

We observed similar signatures of tension and compression due to cell invasion into the fibrous matrix. Within 2–3 hours after encapsulation in fibrin gels, cells begin to develop extensions as they transition from a spherical to a spread phenotype (Fig. 4). During that time, the extensions grow in length as they generate a compacted matrix layer at the periphery of the extension (Fig. 4a and b). The leading edge of the extension, which is often rich in actin (Fig. 4f), is absent from this compacted zone.

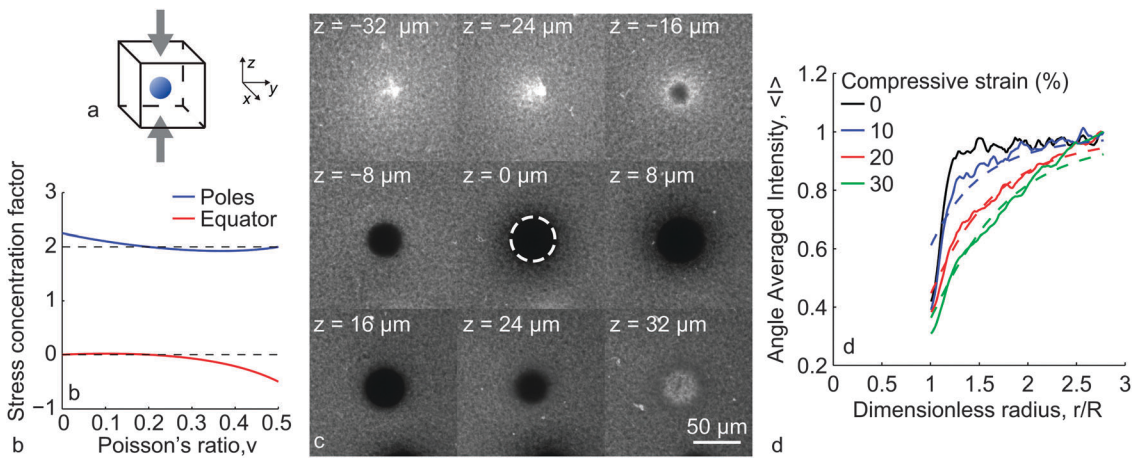

Fig. 3 Signatures of local matrix deformation. (a) A fibrin matrix (3 mg mL^{-1} fibrinogen) with a rigid spherical inclusion (diameter 45 μm) is loaded under compression in the z direction. (b) The stress concentration factor in the matrix on the sphere's surface is computed for the sphere's north/south poles and equator. Since the sphere is under compression, a positive stress concentration factor indicates compression. (c) The fluorescently labeled fibrin matrix is imaged during compression (nominal compressive strain of 30%) and shown at different z position planes. A dotted circle is shown at the equator of the rigid sphere. Fluorescence intensity increases at locations of compression (*e.g.*, $z = -24$ μm, below the sphere) and decreases at locations of tension (*e.g.*, $z = 0$ μm, around the sphere). The asymmetry of the images above and below the midplane ($z = 0$) results from diffraction of light through the sphere when imaging above it. (d) Fluorescence intensity of the matrix is averaged around concentric circles of radial distance r from center of the sphere. Averaging is performed in the x–y plane whose z-coordinate is given by the sphere's equator ($z = 0$ μm). Intensities are normalized to the value far from the sphere and plotted for nominal compressive strains ranging from 0 to 30%. As compressive strain in the z direction increases, tensile strain develops in the xy plane of the matrix, resulting in a decrease in fluorescence signal near the sphere. Dotted lines show fits to the linear elastic scaling $(1 + Cr^{-3})^{-1}$ where C is a constant and r is distance from the sphere (see supplemental note for more detail on this scaling, ESI†).

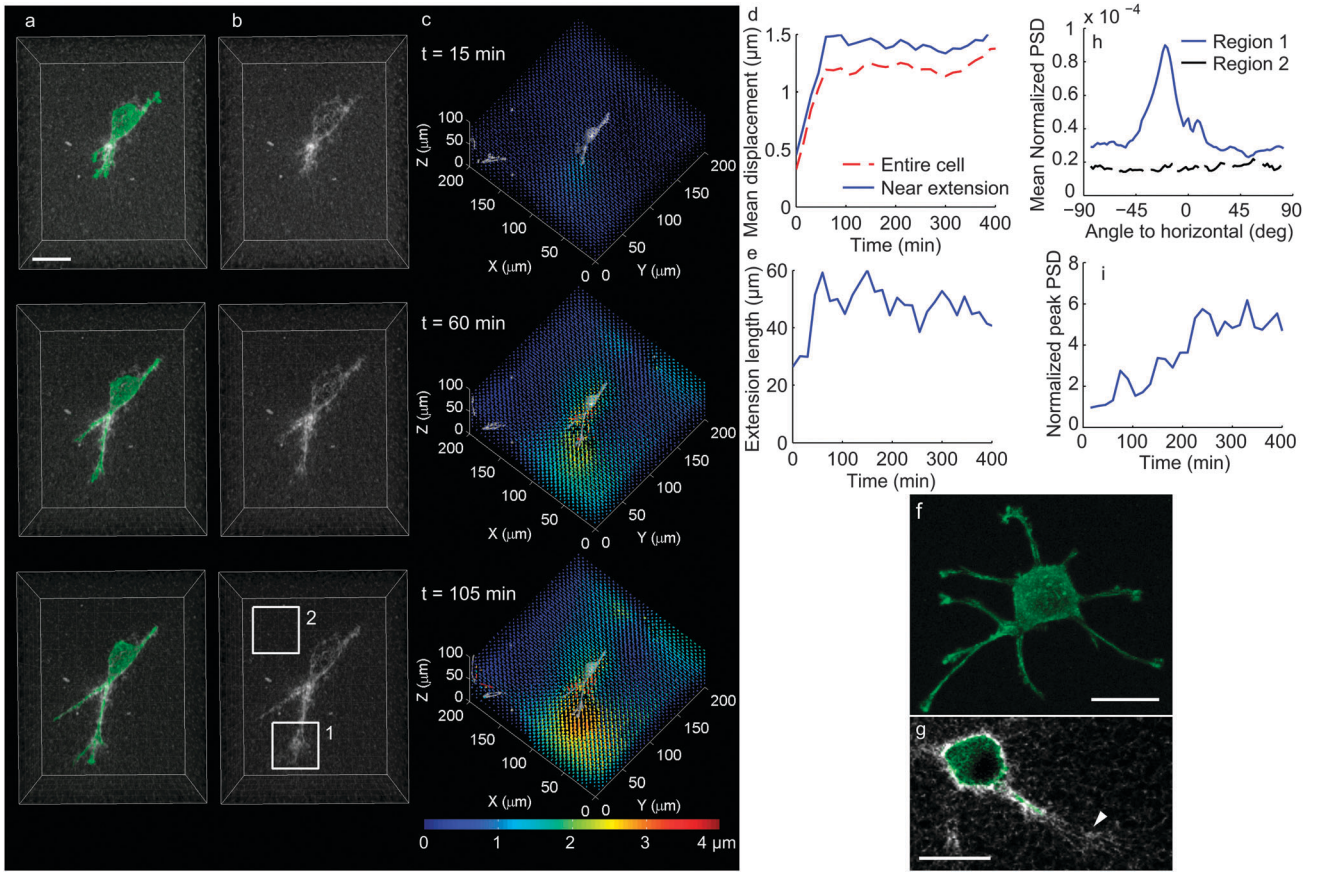

Fig. 4 Time-resolved cell–matrix mechanical interactions during cell invasion. (a, b) Projections of the cell (green) invading into the matrix (gray). Changes in fluorescence intensity over time indicate structural changes within the matrix. (c) Colored quivers show cell-induced displacements in the 3D matrix. (d) The mean of matrix displacements within 50 μm of the cell surface (dotted line) and within 50 μm of the tip of the extension (solid line) increase during the first ~90 min of invasion. (e) The extension grows over a time period of ~90 min. (f) The tips of the cellular extensions are rich with actin. (g) The matrix fibers (gray) in regions around the extension tips (green, actin) are aligned with the direction of the extension (arrow). Times are in minutes after seeding the cells in the matrix; scale bars 20 μm. (h) As the extension grows into the matrix, the fibers align. The alignment is quantified by computing the PSD of different regions in the image. The approximate location of the regions chosen for analysis are labeled in the bottom panel of b; see Fig. S3 (ESI†) for more detail. The peak in the PSD signal at an angle of −20° for region 1 indicates fibers aligned at an angle of 70° to the horizontal. No peak is visible for region 2, indicating an isotropic distribution of fibers. (i) The value of the peak in the PSD signal is normalized by the baseline value of the PSD, away from the peak for region 1, and plotted over time during invasion.

Quantification of the 3D displacements induced by the invading extensions reveals large displacements (3–4 μm) in the volume surrounding the extensions (Fig. 4c). Mean displacements around the cell and around individual extensions increase in proportion to the extension length (Fig. 4d and e) indicating the presence of cell tractions. At the extension tip, and not in other regions along the extension, fibers align with the direction of the leading edge of the extension (Fig. 4g). The fiber alignment indicates the cell pulls on these fibers; regions of fiber compaction (Fig. 4a and b) denote areas where the cell pushes against the matrix. To quantify the dynamics of fiber alignment during invasion, we chose two regions within the matrix (Fig. 4b), and computed the power spectral density (PSD) of the matrix intensity images in each of these regions (Fig. S3, ESI†). Alignment of fibers appeared as bands in the PSD images oriented at an angle of 90° to the angle of fiber alignment. We averaged the PSD images at different angles to compute the relative amount of fiber alignment in different orientations. A sharp peak in the PSD (Fig. 4h) for region 1 was present, indicating highly aligned fibers. The magnitude of the peak grew in time (Fig. 4i) more slowly than the cell extension grew (Fig. 4e), indicating that the cell continued to align matrix fibers even after its extension reached its maximal length.

The compacted zone at the periphery of each extension has a robust fluorescence signal (Fig. 4a and b, gray), which allows us to mark it by an isosurface procedure (see Methods). We then used the volume enclosed by the isosurface to quantify the extent of matrix remodeling during invasion (Fig. 5a). The isosurface takes on the shape of a tube around the cell extension (Fig. 5a), and thus the volume is nearly linearly proportional to its length. We therefore compare the volume of the isosurface to the extension length, and we detect two distinct behaviors. Initially, as the extension grows (typically the first 50–100 min), the remodeled matrix volume increases at a similar rate to the rate of increase in the extension's length (Fig. 5b and c). However, as the extension retracts (typically after 50–100 min), the volume of the remodeled matrix decreases at a slower rate

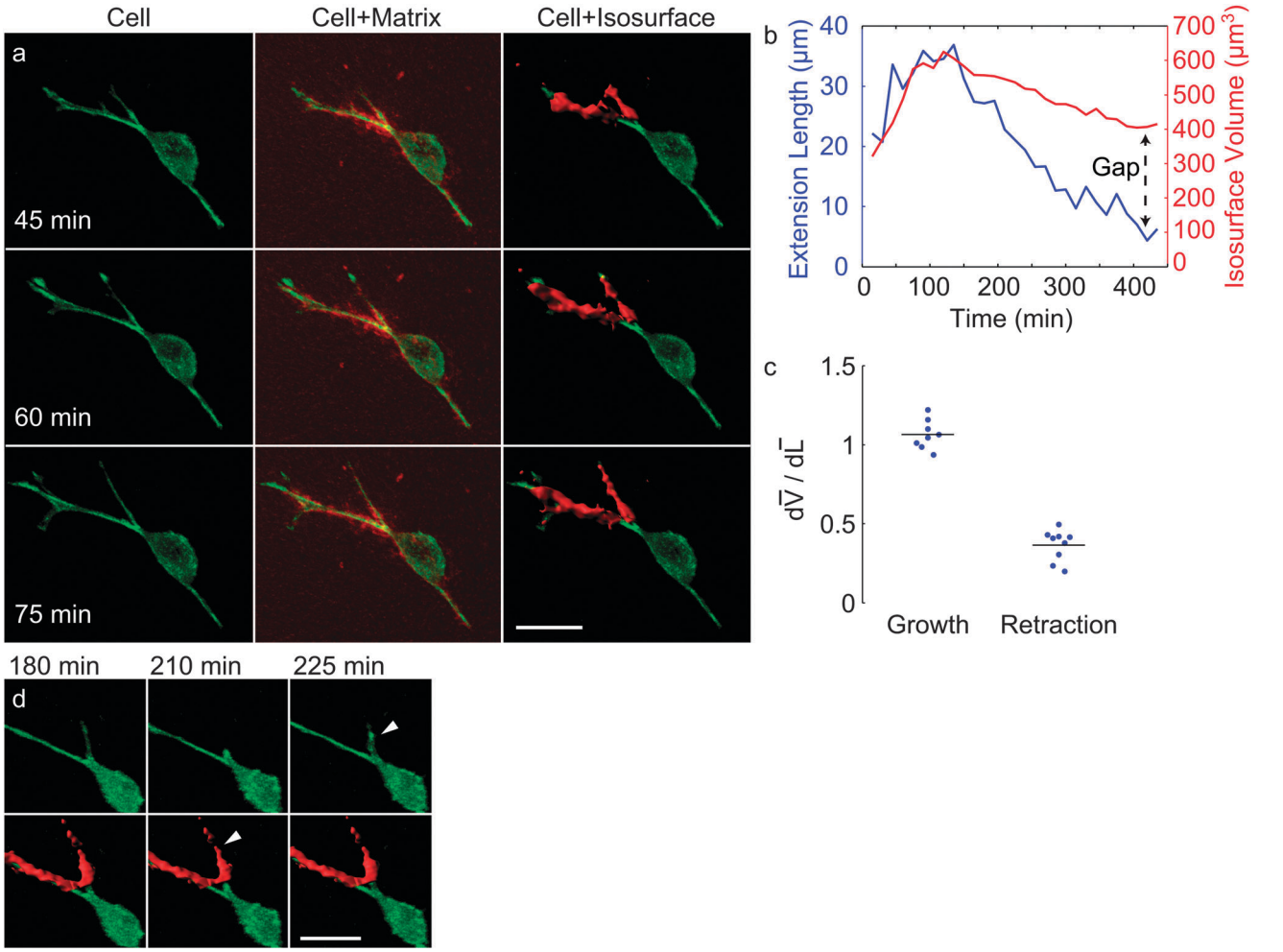

Fig. 5 Quantification of matrix structural remodeling. The cell (labeled with actin-GFP) is in green in all panels. (a) An isosurface analysis (right panels) is used to quantify the volume of the deformed matrix over time during cell invasion in the fibrous matrix. The center panels show the labeled fibrin matrix in red. (b) Quantification of the isosurface volume and extension length during cell invasion. In the course of retraction of the extension (after 150 min), the volume enclosed by the isosurface decreases at a slower rate than the extension length leaving a gap between the curves of extension length and isosurface volume. This gap indicates plastic deformation of the matrix. (c) For multiple cell extensions, the normalized matrix isosurface volume $\bar{V}$ and extension length $\bar{L}$ are computed by dividing by the maximum values of volume and length, respectively. The derivative $d\bar{V}/d\bar{L}$ is then computed using a linear fit to the data during extension growth and retraction. During retraction, $d\bar{V}/d\bar{L} \sim 0.4$, indicating $\sim$40% of the matrix remains permanently deformed. (d) Deformation of the matrix is permanent, leaving an isosurface track after retraction of the cellular extension (arrow, 150 min). The extension re-grows into the plastically-deformed matrix cavity (arrow, 160 min). Scale bars 20 μm.

than the cell extension length as indicated by a "gap" in Fig. 5b. This gap remains indefinitely after the cell extension retracts, indicating plastic, irreversible deformation of the matrix. By calculating the change in isosurface volume with respect to the change in extension length (Fig. 5c), we estimate $\sim$40% plastic deformation. We find the value of 40% to be typical for extensions of multiple cells invading over the time scales of our experiments (5–6 h). Thus, during invasion, cells create significant permanent deformation in the matrix. Compared to unstressed matrix, these plastically deformed regions have different mechanical properties and microstructure, which may impact cell behavior. Indeed, we noticed that many of the retracted extensions re-grow into the tubular structures of the matrix (Fig. 5d).

Because the cell displaces the matrix as it invades, the regions of matrix compaction result from cell-generated forces. To estimate these forces, we further analyzed the 3D displacement field within the matrix. Since our experimental approach quantifies matrix displacements throughout the imaging volume, a numerical computation of the gradient of the displacement field yields the strain tensor at all locations within the matrix[28,29] with accuracy of $\sim$0.1% strain (Fig. 1c and Fig. S1, ESI†). Analyzing strains within the matrix offers an advantage over analyzing displacements in that strains report the relative increase or decrease in matrix deformation. Therefore, even without knowing the constitutive properties of the matrix, we can infer details about the state of stress within the matrix by examining the strain. For example, if strain is negative (positive), the matrix is under compression (tension), even if the exact magnitude of the compressive force is unknown. Thus, matrix strains relate to the forces applied by the cell more closely than matrix displacements.

A further advantage of our direct computation of strains is that it does not require solving an inverse problem as in 2D TFM[30–32] or recent implementations of 3D TFM.[9] In three dimensions, these inverse problems are sensitive to the outline of the cell and are subject to errors of greater than 30%.[33]

We interpret matrix strains in the context of the cellular forces by quantifying regions near the cell where matrix strains are large (where we define "large" as greater than 2% strain). We start by computing strains normal to the cell, which allows us to distinguish between regions of tension and compression within the matrix. We look specifically at the interface between the cell and the matrix. At this interface, the areas of tensile and compressive strain correlate to locations where the cell is pulling and pushing on the matrix. We find that cells in fibrous matrices apply both pulling and pushing forces (Fig. 6a and b). For multiple different cells, areas of pulling forces are of roughly the same order of magnitude as areas of pushing forces (Fig. 6b). Although the location of pulling and pushing forces changes over time, pushing forces often appear near the cell body and pulling forces appear along the leading edges of extensions (Fig. 7). At various time points, we also observed pushing forces near the tip of a growing cell extension (Fig. 7, t = 150 min), indicating that the cell can locally push matrix fibers aside as its extension grows.

Our strain analysis also allows us to distinguish between matrix deformations normal and tangent to the cell surface. In contrast to a previous study,[9] we find approximately equal areas of normal and tangent (shear) cell-induced matrix strains (Fig. 6c), indicating the cell applies a combination of normal and shearing forces. Along the cell's invading extension, areas applying inward normal forces to the matrix (Fig. 6d) are larger than either outward normal forces (Fig. 6d) or shearing forces (Fig. 6e). The spatial distribution of inward and outward forces covers nearly continuous areas that varied smoothly along the cell's surface indicating a coupling of pulling and pushing forces. An inward force-generating area, for example, could induce an outward force in a proximal area due to a change in cell's geometry and the requirement of mechanical equilibrium.

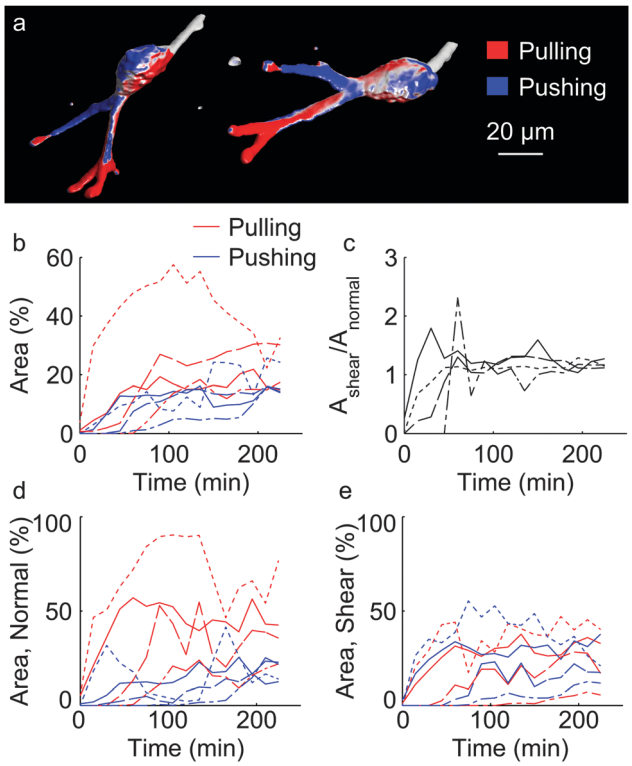

Fig. 6 Matrix strains reveal pulling and pushing forces. (a) Tensile and compressive strains in the matrix next to the cell surface indicate regions where the cell applies large pulling and pushing forces (corresponding to >2% strain), respectively. These regions are colored and plotted on the surface of the cell. (b) Areas on the cell surface applying large pulling and pushing forces are computed and normalized by the total cell surface area. These normalized areas are plotted as a percentage over time for both the pulling and pushing directions. Each line pattern corresponds to a different cell. (c) Matrix regions near the cell surface under shear and normal strain indicate regions where the cell applies shear and normal forces. Cell surface areas exhibiting large shearing and normal forces are computed and their ratio is plotted over time for multiple cells. Relative surface areas on individual extensions exhibiting normal and shearing forces are plotted in (d) and (e), respectively.

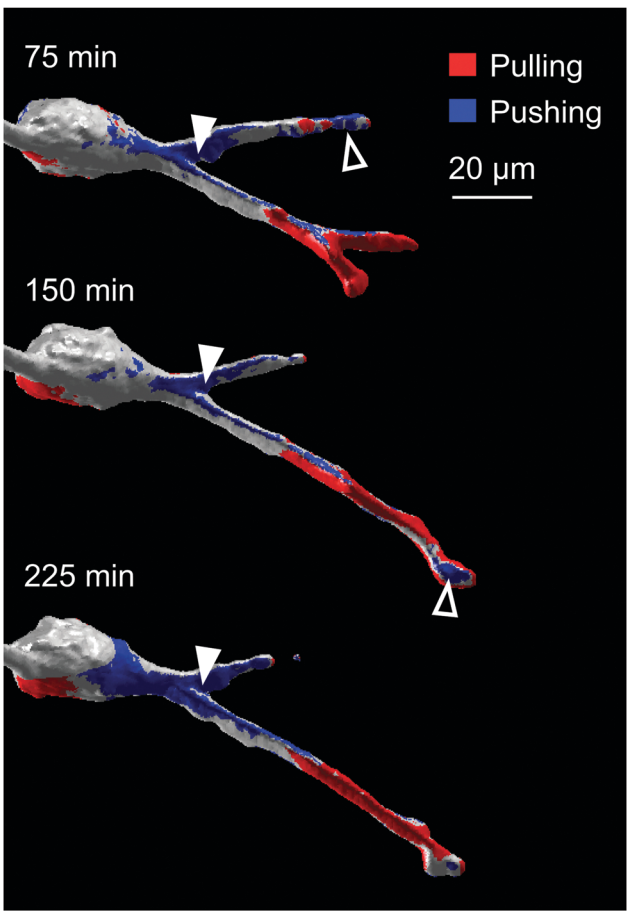

Fig. 7 Spatiotemporal location of pulling and pushing forces. An invading cell generally applies pulling forces (red) to the matrix near the leading edge of the extension and pushing forces (blue) near the cell body, where the cross sectional diameter of the extension is larger. Pushing forces are also evident in sites where an extension splits (solid arrows) or at the tip of a growing extension (hollow arrows). The locations of pulling and pushing forces we show here are typical for multiple different cells.

Discussion

Most previous studies that quantified cell tractions in 2D[30,31] and recently in 3D systems[9,15,34] relied on tracking fluorescent particles embedded in the gel. While these techniques have yielded important understanding of cell–matrix mechanical interactions, they have not provided detailed information about cell-induced structural rearrangement of matrix fibers.[15–18,35] Such details are integral to revealing local variations in the extracellular matrix and their possible effect on cell function. In addition, incorporation of micron-sized particles into the matrix can influence gel mechanical properties and may introduce errors due to Brownian motion of particles that are not bound to fibers. Our technique circumvents the use of particles, and reports 3D displacements and strains while documenting structural modification of the matrix such as fiber densification, compaction and alignment. The precision and accuracy of our displacement measurements are similar to those obtained by correlating images of particles (Fig. S1, ESI†), and compare favorably to the results of previous studies that tracked individual fluorescent particles, which reported errors of $\sim$1 μm[9] and $\sim$0.1 μm.[14]

Here, by combining imaging of matrix fibers and DVC to measure displacement fields, we examined the process of cell invasion into a 3D fibrin matrix. To invade a fibrous matrix, cells squeeze through gaps in the fiber meshwork and displace or degrade impeding matrix fibers.[36] To quantify how the cell remodels the matrix to invade, we applied our ''2-in-1'' experimental approach, which provides information on both deformation and structural reorganization of the matrix. In our experiments, we followed cell invasion 2–6 hours after seeding the cells. This time scale is short compared with time scales for matrix remodeling by proteolytic degradation, which have been suggested to be over 24 hours.[25] In regions where the cell invades into the matrix, fibers become compacted, changing the local distribution of fluorescence intensity. Such changes can potentially create errors in computing matrix displacements using DVC, but our numerical simulations indicate that as long as $<$3% of a subvolume is changed (either due to fiber densification or degradation), errors are minimal (Fig. S2, ESI†). For cell invasion experiments, we estimate that the maximal possible volume occupied by the highly densified matrix can reach a similar value (3.6 $\pm$ 0.6% of a subvolume, Fig. S2d, ESI†), indicating that formation of densified matrix regions over time has minimal effect on measuring cell-induced displacements. Computing displacements with DVC requires a volume stack of the matrix in a stress-free reference state. Frequently in cell traction experiments, this reference is achieved by inhibiting cell force at the end of the experiment (*e.g.*, by using blebbistatin). In our experiments, the fibrous matrix deforms both elastically and plastically, so treatment with blebbistatin would only allow for measuring the elastic deformation. To circumvent this issue, we began imaging shortly after seeding the cells in the matrix. Because the matrix remained undeformed before the cells began to spread, we used this first imaging time point as the stress-free reference state.

We identified two main structural signatures of matrix reorganization by invading cells: compaction of fibers at the sides of advancing cell extensions; and alignment of fibers at the leading edges of the extensions. Approximately half of the affected matrix deformed plastically, leaving tube-like matrix gaps with available space for subsequent growth of cell extensions. Previous studies have described larger-scale tracks in 3D collagen matrices that are created by proteolytic degradation of matrix fibers, which stimulate collective invasion of tumor cells.[16] The micro-tunnels observed here could also form, at least in part, by fiber degradation, but our simultaneous observation of matrix displacement and compaction around cell extensions suggests that plastic deformation also contributes to generating matrix cavities. From this finding, we conclude that matrix plasticity can direct and control cell morphology and migration.

Our analysis of cell invasion reveals the location and direction of forces applied by the invading cell. Previous studies have reported deformations of fibrous matrices in terms of scalar quantities.[13,14,37] Such scalars provide a useful metric for global strains, but they are of limited use in quantifying local deformations. Indeed, our finding that cells push against the matrix while invading required localized analysis of matrix strains along the cell's invasive extension. Using strain to quantify cell–matrix interactions offers the advantage that the constitutive behavior of the fibrous matrix is not required. Rather than using strains, a previous study by Koch *et al.*[14] quantified strain energy within the matrix by assuming a homogeneous, linear, elastic constitutive relationship. However, the equations of linear elasticity do not account for the time-dependent properties we observe here, such as viscoelasticity (Fig. 2) and plasticity (Fig. 5). They also do not account for inhomogeneous constitutive properties, which are typical in fibrous materials.[38] Moreover, even for small deformations, fibrous materials exhibit nonlinearity due to buckling in compression.[24] While Koch *et al.* point out that their approach can be easily improved with more accurate constitutive relationships, further research is required to develop accurate constitutive relationships for fibrous matrices.

Because the actomyosin network applies force by contracting, a logical assumption is that cells can only pull against the matrix; they cannot push. Our analysis of the 3D strains within the matrix revealed the presence of such pulling forces, but, surprisingly, we also found pushing forces. Recent studies have observed pushing forces on a flat substrate, for example, under the nucleus of migrating amoeba *Dictyostelium discoideum*[39] or at the leading edge of migrating fibroblasts.[5] In three dimensions, pushing forces have resulted from the collective action of multicellular structures,[9,15] but pushing forces applied by single cells within a fibrous matrix have not yet been observed. Nevertheless, previous studies have predicted that cells push against ring-like fibrous ''belts'' surrounding the invading cell[18] and that such pushing forces help the cell to degrade the matrix by putting matrix fibers in direct contact with proteolytic enzymes attached to the cell membrane.[17] These predictions of cells pushing against fibrous belts imply a force balance mechanism that begins when a cell adheres to the matrix with a slender extension and contracts using the actomyosin machinery. This contractile force must be

balanced to achieve force equilibrium, and the balancing force results from the cell body becoming compressed against matrix fibers where the cell diameter is too large to fit through the pores in the fibrous meshwork. Some of the pushing forces that we observe are located near the cell body, where the cell size is larger (Fig. 7). Thus our quantitative measurements of pushing forces near the cell body agree with previous experimental studies[17,18] on cell invasion. Yet surprisingly we also often observe pushing forces at the leading edge of a cell extension. At this leading edge, pushing could not result from a global force balance, as it could near the cell body, and therefore these pushing forces must result from a different mechanism than actomyosin contraction. Potential mechanisms are microtubule compression,[40] actin polymerization,[41] and increased intracellular pressure.[42] Further experiments to inhibit cytoskeletal proteins such as actin or microtubules can shed light on the mechanism underlying how cells push against the matrix.

The pushing forces we observe (Fig. 6) indicate that compressive forces are present within the cell. Like the actin fibers inside the cell, the inhomogeneous matrix fibers outside the cell buckle under compression.[24] Thus, achieving substantial compressive strains near the cell surface does not require large compressive force within the cell: the nonlinear behavior of the fibrous matrix likely facilitates cell pushing by offering less resistance to compression than to tension. This nonlinearity, which is specific to fibrous materials, may explain why we observe cell pushing in a fibrous matrix, whereas a previous study in synthetic linear gels did not:[9] the synthetic gels were likely far stiffer in compression than the fibrous matrix we used here.

In summary, we have developed a real-time, 3D technique capable of quantifying matrix displacements, strains, and structural consequences of matrix remodeling in the context of cell invasion. The technique uses direct 3D fluorescence imaging of the fibrous network, and provides a promising platform to investigate cellular interaction with native, physiologically relevant extracellular matrices. While we use fibrin as a matrix here, our technology can be easily adapted to collagen or a different fibrous material to investigate other cellular processes. Furthermore, since the DVC requires only an inhomogeneous pattern for measuring displacements and strains, this technique can be extended to label free imaging of the fibrous matrix, such as confocal reflection microscopy or second harmonic generation microscopy. We expect the flexibility of our method to provide new insight regarding how the extracellular matrix participates in mechanical signaling to dictate cell fate and thereby elucidate mechanotransduction mechanisms in three dimensions. We further expect our technique to open up new directions in measuring forces and matrix remodeling events in live organisms by using the native extracellular matrix as a probe for real-time tracking.

Experimental methods

Cell culture

NIH 3T3 fibroblasts (passages 10–20) stably expressing GFP-actin were cultured in DMEM medium supplemented with 10% fetal bovine serum and 1× non-essential amino acids in a 37 °C humid incubator.

Fibrin gel preparation and fluorescent labeling

Human fibrinogen solution (Omrix Biopharmaceuticals, Israel) was covalently labeled with a fluorescent dye before fibrin gel preparation. Alexa Fluor 546 coupled to an amine-reactive succinimidyl ester (Invitrogen) was mixed with fibrinogen solution in a 5 : 1 dye-to-protein molar ratio for 1 hour at room temperature and then filtered through a HiTrap desalting column packed with Sephadex G-25 resin (GE Healthcare, Milwaukee, WI) to separate the unreacted dye. The dye was chosen to have a relatively high fluorescence quantum yield (~80%) in order to minimize undesirable gel drift caused by heat dissipation. Aliquots of labeled fibrinogen were stored at −20 °C and thawed before use. To create the fibrin cellular constructs, NIH 3T3 fibroblasts expressing GFP-actin (3000 cells) were suspended in 10 μL of a 20 U mL^{-1} solution of thrombin (Omrix Biopharmaceuticals, Israel). The thrombin-cell suspension was placed on a #1.5 cover-slip attached to a 35 mm dish (MatTek, Ashland, MA), and mixed gently with 10 μL labeled-fibrinogen solution. The resulting fibrin gel was placed in the incubator for 20 minutes to fully polymerize, after which warm medium was added to cover the gel.

Fibrin gel characterization

The constitutive mechanical properties of fibrin gels (4 mg mL^{-1} of fluorescently-labeled fibrinogen, as was used for the cell experiments) were measured using a stress-controlled AR1000 rheometer (TA Instruments, New Castle, DE) equipped with 8 mm diameter aluminum parallel plates. The temperature was set to 37 °C. Stress sweep tests were initially performed to evaluate the stress in the linear region appropriate for the frequency sweep tests. For the frequency sweeps, a stress of 4 Pa and a frequency range of 0.1–1 rad s^{-1} were applied. The fibrin gel was prepared on the rheometer while sandwiched between two sheets of sandpaper to avoid slipping. After 20 minutes of polymerization, warm PBS was added to cover the gel, and a wet sponge was placed around the gel to prevent drying. Six different samples were included in the analysis.

Confocal microscopy

For the images presented in Fig. 1, a Swept Field confocal microscope mounted on a Ti stand (Nikon Instruments, Melville, NY) was used. A 40× NA 1.15 water immersion objective was used due to the match in index of refraction of the immersion medium and the water-based fibrin gel. Images were captured with a QuantEM:512SC camera (Photometrics, Tucson, AZ). Volume stacks were collected with an out-of-plane (z) step size of 0.4 μm. The microscope was housed in a custom-built chamber heated with an Air-Therm ATX heater (World Precision Instruments, Sarasota, FL) to 37 °C. CO_2 was maintained at 5% by circulating 5% CO_2 in air within the chamber.

For the time-lapse experiments with cells and control experiments without cells, we used an LSM 710 microscope (Carl Zeiss) in two-photon laser scanning mode at a wavelength of 900 nm

in multiple x–y positions. Two-photon imaging was found to be less phototoxic than confocal imaging during cell spreading. The 900 nm wavelength allowed imaging of the Alexa Flour 546-labeled fibrin matrix and GFP-actin cells simultaneously. Volume stacks were collected every 10 min with a z step size of 0.4 μm for 6 hours. The microscope chamber and the stage were heated to 37 °C. CO_2 was maintained at 5%. A 40× 1.2 NA Apochromat water immersion objective lens (Carl Zeiss) was used. At the end of the experiment, 85 μM blebbistatin (Sigma-Aldrich, St. Louis, MO) was added to the cell culture medium to arrest cellular contraction and allow the fibrin matrix to recover. Additional volume stacks were then collected for 2 hours and used as a reference for DVC. For cell invasion experiments, no blebbistatin was used, because the cells were imaged within 3 hours after seeding in the fibrin gels. The stress-free reference was thus taken to be the first stack collected in these experiments.

Displacement and strain computation

Before computing displacements, a deconvolution algorithm was used to improve the resolution in the axial (z) direction as described previously.[20] Displacements were computed using a DVC algorithm as described previously.[10,20] An updated version of the DVC software, written in Matlab (The Mathworks, Natick, MA), is now freely available online.[43] The DVC subvolumes contained 64 × 64 × 64 voxels (25 × 25 × 25 μm) at a spatial resolution of 16 voxels. To compute cumulative matrix displacements, volume stacks were compared to a reference state achieved by adding 85 μM blebbistatin to the cell culture medium (for static experiments, Fig. 1) or by imaging immediately after suspending the cells in the fibrin gels (for spreading experiments, Fig. 4). Strain tensor components were computed numerically from the displacement data throughout the image volume by fitting a 3 × 3 × 3 grid of points to a 3D linear function, as illustrated for one strain component in Fig. S4 (ESI†), and as described previously.[20]

During control experiments the gels contracted, creating nonzero diagonal components of the strain tensor. The effects of gel contraction were compensated by computing average normal strains within the image stack. The displacements were then corrected so that normal strains in each volume stack equaled zero. Finally, drift in the experiment resulting in rigid body translation of the image volume was eliminated by translating the displacement data so that the medians of each displacement component were zero.

Our procedure for analyzing strains near the cell is summarized in Fig. S4c (ESI†). We first identified vectors normal to the cell surface by smoothing the cell image with a 3 × 3 × 3 voxel averaging filter and then computing an isosurface of the cell in Matlab. The isosurface generated a mesh of vertices and faces representing the cell surface separated by ~1 voxel. The unit outward normal vector $\mathbf{n}$ for each face was computed, and matrix strains in the direction normal to the cell were computed with the tensor product $\mathbf{n}\cdot\boldsymbol{\varepsilon}\cdot\mathbf{n}$ where $\boldsymbol{\varepsilon}$ is the strain tensor. Shearing strains were computed using the tensor product $\mathbf{v}\cdot\boldsymbol{\varepsilon}\cdot\mathbf{n}$. For computing shearing strains along a cell extension, $\mathbf{v}$ is a unit vector in the direction of the cell extension; for shearing strains around the cell body, $\mathbf{v} = \mathbf{1} - \mathbf{n}$, where $\mathbf{1}$ is the vector (1,1,1). Because the noise in the strain measurement is ~0.1% (Fig. S1, ESI†) and noise in computing the normal vectors $\mathbf{n}$ will amplify errors, only regions of the cell applying large strain, defined as greater than 2%, to the matrix were analyzed. The area of each cell in contact with matrix under large strain (>2%) was summed and normalized by the total surface area of the cell.

Matrix isosurface measurements

Isosurface analysis was performed with Imaris (version 7.6.4; Bitplane) using the ''surfaces'' tool. Background subtraction was initially performed. A fluorescent threshold was manually chosen to capture the voxels with intensities greater than the 5th percentile. This threshold value was found to capture most of the remodeled matrix around the cellular extension, whereas the undeformed matrix away from the cell usually exhibited intensity below the 5th percentile. The same threshold was used in all experiments. All voxels with fluorescence intensities above the threshold were marked by the isosurface, and used for the deformed matrix volume analysis.

The experiments in Fig. S2 (ESI†) required an estimate of the maximal volume of densified matrix within a 64 × 64 × 64 voxel subvolume. For this estimate, we measured the volume of the isosurface around cell extensions (n = 8) with length of 45 μm. This length corresponds to the maximum length that can fit into the 64 × 64 × 64 voxel subvolume.

Extension length measurements

The length of the extension was calculated with Imaris using the ''filament'' tool. The beginning and end of the extension were manually chosen at each time point and the length was thereafter calculated using the software.

Matrix fiber alignment analysis

Alignment of the matrix fibers was analyzed with a Fourier transform based technique similar to techniques described previously.[44] To simplify visualization of the results, the analysis was performed on maximum intensity projections of the 3D volume stacks of the matrix images. The power spectral densities (PSDs) of selected regions of the fibrin matrix were computed in Matlab. The PSD for each region was normalized by the number of pixels in each region of interest times the sum of the square of the intensity of each pixel in the region of interest. Matrix fiber alignment appeared in the PSD images as a band oriented at an angle of 90° to the angle of fiber alignment. Mean values, computed along a ray drawn from the center of the PSD image to the edge, were computed for various angles to the horizontal. Central PSD values were not used in computing the mean, because these values were affected by long wavelength characteristics such as image brightness.

Acknowledgements

We thank Scott Fraser for providing the transfected fibroblasts. We thank the Biological Imaging Center of the Beckman Institute at Caltech for use of the two-photon microscope.

This work was funded by grants from the National Science Foundation (Division of Materials Research 0520565 and 1206121) and from the California Institute for Regenerative Medicine (RB5-07398). J.N. was supported by the National Science Foundation Graduate Research Fellowship under Grant No. DGE-1144469. A.L. was supported in part by a Rothschild Foundation fellowship. We thank Samuel A. Safran and Xinpeng Xu for reviewing the paper and providing useful comments.

References

1 L. G. Griffith and M. A. Swartz, *Nat. Rev. Mol. Cell Biol.*, 2006, **7**, 211–224.
2 S. Munevar, Y. Wang and M. Dembo, *Biophys. J.*, 2001, **80**, 1744–1757.
3 E. Paluch and C. P. Heisenberg, *Curr. Biol.*, 2009, **19**, R790–R799.
4 K. R. Levental, H. M. Yu, L. Kass, J. N. Lakins, M. Egeblad, J. T. Erler, S. F. T. Fong, K. Csiszar, A. Giaccia, W. Weninger, M. Yamauchi, D. L. Gasser and V. M. Weaver, *Cell*, 2009, **139**, 891–906.
5 S. A. Maskarinec, C. Franck, D. A. Tirrell and G. Ravichandran, *Proc. Natl. Acad. Sci. U. S. A.*, 2009, **106**, 22108–22113.
6 S. S. Hur, Y. H. Zhao, Y. S. Li, E. Botvinick and S. Chien, *Cell. Mol. Bioeng.*, 2009, **2**, 425–436.
7 W. R. Legant, C. K. Choi, J. S. Miller, L. Shao, L. Gao, E. Betzig and C. S. Chen, *Proc. Natl. Acad. Sci. U. S. A.*, 2013, **110**, 881–886.
8 J. Notbohm, J. H. Kim, A. R. Asthagiri and G. Ravichandran, *Biophys. J.*, 2012, **102**, 1323–1330.
9 W. R. Legant, J. S. Miller, B. L. Blakely, D. M. Cohen, G. M. Genin and C. S. Chen, *Nat. Methods*, 2010, **7**, 969–971.
10 A. Lesman, J. Notbohm, D. A. Tirrel and G. Ravichandran, *J. Cell Biol.*, 2014, **205**, 155–162.
11 K. M. Riching, B. L. Cox, M. R. Salick, C. Pehlke, A. S. Riching, S. M. Ponik, B. R. Bass, W. C. Crone, Y. Jiang, A. M. Weaver, K. W. Eliceiri and P. J. Keely, *Biophys. J.*, 2014, **107**, 2546–2558.
12 R. J. Bloom, J. P. George, A. Celedon, S. X. Sun and D. Wirtz, *Biophys. J.*, 2008, **95**, 4077–4088.
13 A. M. Pizzo, K. Kokini, L. C. Vaughn, B. Z. Waisner and S. L. Voytik-Harbin, *J. Appl. Physiol.*, 2005, **98**, 1909–1921.
14 T. M. Koch, S. Munster, N. Bonakdar, J. P. Butler and B. Fabry, *PLoS One*, 2012, **7**, e33476.
15 N. Gjorevski and C. M. Nelson, *Biophys. J.*, 2012, **103**, 152–162.
16 K. Wolf, Y. I. Wu, Y. Liu, J. Geiger, E. Tam, C. Overall, M. S. Stack and P. Friedl, *Nat. Cell Biol.*, 2007, **9**, 893–904.
17 P. Friedl and K. Wolf, *Cancer Metastasis Rev.*, 2009, **28**, 129–135.
18 K. Wolf and P. Friedl, *Clin. Exp. Metastasis*, 2009, **26**, 289–298.
19 L. M. Jawerth, S. Munster, D. A. Vader, B. Fabry and D. A. Weitz, *Biophys. J.*, 2010, **98**, L1–L3.
20 C. Franck, S. Hong, S. A. Maskarinec, D. A. Tirrell and G. Ravichandran, *Exp. Mech.*, 2007, **47**, 427–438.
21 D. E. Discher, P. Janmey and Y. L. Wang, *Science*, 2005, **310**, 1139–1143.
22 C. Storm, J. J. Pastore, F. C. MacKintosh, T. C. Lubensky and P. A. Janmey, *Nature*, 2005, **435**, 191–194.
23 A. E. Brown, R. I. Litvinov, D. E. Discher, P. K. Purohit and J. W. Weisel, *Science*, 2009, **325**, 741–744.
24 J. Notbohm, A. Lesman, P. Rosakis, D. A. Tirrel and G. Ravichandran, *J. R. Soc., Interface*, 2015, 20150320, DOI: 10.1098/rsif.2015.0320.
25 K. A. Jansen, R. G. Bacabac, I. K. Piechocka and G. H. Koenderink, *Biophys. J.*, 2013, **105**, 2240–2251.
26 K. Wolf and P. Friedl, *Trends Cell Biol.*, 2011, **21**, 736–744.
27 J. N. Goodier, *J. Appl. Mech.*, 1933, **1**, 39–44.
28 C. Franck, S. A. Maskarinec, D. A. Tirrell and G. Ravichandran, *PLoS One*, 2011, **6**, 15.
29 J. Toyjanova, E. Bar-Kochba, C. Lopez-Fagundo, J. Reichner, D. Hoffman-Kim and C. Franck, *PLoS One*, 2014, **9**, 1–12.
30 M. Dembo and Y. L. Wang, *Biophys. J.*, 1999, **76**, 2307–2316.
31 J. P. Butler, I. M. Tolic-Norrelykke, B. Fabry and J. J. Fredberg, *Am. J. Physiol.: Cell Physiol.*, 2002, **282**, C595–C605.
32 J. C. del Alamo, R. Meili, B. Alonso-Latorre, J. Rodriguez-Rodriguez, A. Aliseda, R. A. Firtel and J. C. Lasheras, *Proc. Natl. Acad. Sci. U. S. A.*, 2007, **104**, 13343–13348.
33 G. Vitale, L. Preziosi and D. Ambrosi, *Inverse Probl.*, 2012, **28**, 095013.
34 M. D. Lopez-Garcia, D. J. Beebe and W. C. Crone, *Ann. Biomed. Eng.*, 2010, **38**, 2485–2498.
35 C. M. Kraning-Rush, S. P. Carey, J. P. Califano, B. N. Smith and C. A. Reinhart-King, *Phys. Biol.*, 2011, **8**, 015009.
36 P. Friedl and K. Wolf, *J. Cell Biol.*, 2010, **188**, 11–19.
37 B. A. Roeder, K. Kokini, J. P. Robinson and S. L. Voytik-Harbin, *J. Biomech. Eng.*, 2004, **126**, 699–708.
38 M. A. Kotlarchyk, S. G. Shreim, M. B. Alvarez-Elizondo, L. C. Estrada, R. Singh, L. Valdevit, E. Kniazeva, E. Gratton, A. J. Putnam and E. L. Botvinick, *PLoS One*, 2011, **6**, e20201.
39 H. Delanoe-Ayari, J. P. Rieu and M. Sano, *Phys. Rev. Lett.*, 2010, **105**, 248103.
40 S. Rhee, H. Jiang, C. H. Ho and F. Grinnell, *Proc. Natl. Acad. Sci. U. S. A.*, 2007, **104**, 5425–5430.
41 G. G. Borisy and T. M. Svitkina, *Curr. Opin. Cell Biol.*, 2000, **12**, 104–112.
42 R. J. Petrie, H. Koo and K. M. Yamada, *Science*, 2014, **345**, 1062–1065.
43 E. Bar-Kochba, J. Toyjanova, E. Andrews, K.-S. Kim and C. Franck, *Exp. Mech.*, 2015, **55**, 261–274.
44 S. Chaudhuri, H. Nguyen, R. M. Rangayyan, S. Walsh and C. B. Frank, *IEEE Trans. Biomed. Eng.*, 1987, **34**, 509–518.